

GRB 210217A: A short or a long GRB?

Dimple^{1,2,*}, Kuntal Misra¹, Ankur Ghosh^{1,3}, K. G. Arun⁴, Rahul Gupta^{1,2}, Amit Kumar^{1,3}, L. Resmi⁵, S. B. Pandey¹ and Lallan Yadav²

¹Aryabhata Research Institute of Observational Sciences (ARIES), Manora Peak, Nainital-263002, India.

²Department of Physics, Deen Dayal Upadhyaya Gorakhpur University, Gorakhpur-273009, India.

³School of Studies in Physics and Astrophysics, Pt. Ravishankar Shukla University, Chattisgarh 492010, India.

⁴Chennai Mathematical Institute, Siruseri, 603103 Tamilnadu, India.

⁵Indian Institute of Space Science and Technology, Trivandrum 695 547, India.

*Corresponding author. E-mail: dimple@aries.res.in

MS received 2021; accepted —

Abstract. Gamma-ray bursts are traditionally classified as short and long bursts based on their T_{90} value (the time interval during which an instrument observes 5% to 95% of gamma-ray/hard X-ray fluence). However, T_{90} is dependent on the detector sensitivity and the energy range in which the instrument operates. As a result, different instruments provide different values of T_{90} for a burst. GRB 210217A is detected with different duration by *Swift* and *Fermi*. It is classified as a long/soft GRB by *Swift*-BAT with a T_{90} value of 3.76 sec. On the other hand, the sub-threshold detection by *Fermi*-GBM classified GRB 210217A as a short/hard burst with a duration of 1.024 sec. We present the multi-wavelength analysis of GRB 210217A (lying in the overlapping regime of long and short GRBs) to identify its actual class using multi-wavelength data. We utilized the T_{90} -hardness ratio, T_{90} - E_p , and T_{90} - t_{mvt} distributions of the GRBs to find the probability of GRB 210217A being a short GRB. Further, we estimated the photometric redshift of the burst by fitting the joint XRT/UVOT SED and place the burst in the Amati plane. We found that GRB 210217A is an ambiguous burst showing properties of both short and long class of GRBs.

Keywords. gamma-ray burst: general, gamma-ray burst: individual: GRB 210217A, methods: data analysis

1. Introduction

Gamma-ray bursts (GRBs) are the short and intense pulses of γ -rays, occurring randomly at a rate of ~ 1 event per day. The bi-modality in T_{90} distribution of GRBs is used to divide these energetic events into two classes: short and long bursts with a boundary at 2 sec (Kouveliotou et al., 1993). However, the T_{90} value relies on the energy range in which the instrument operates and its trigger method. In general, bursts have a lower value of T_{90} in higher energy channels (Qin & Chen, 2013; Fenimore et al., 1995). The T_{90} value also depends on the sensitivity of the detector and background variations. Further, the observed T_{90} depends on the redshift; the rest frame duration ($T_{90}/(1+z)$) will be lower than the observed. It is challenging to decide the class of the GRB without any redshift information. It is also observed that some GRBs with T_{90} values favourable to long GRBs have afterglow and host properties similar to the short GRBs (Gal-Yam et al., 2006). On the other hand, other GRBs with T_{90} less than 2 sec

show properties identical to long GRBs (Antonelli et al., 2009; Ahumada et al., 2021).

Therefore, it is difficult to classify the GRBs based on T_{90} alone, particularly for GRBs lying close to the boundary. It is also essential to look for other observational characteristics apart from their T_{90} information that can distinguish the two classes.

Hardness ratio (HR), the fluence ratio in harder to softer energy bands, can be used to classify GRBs. Short GRBs are found to be harder with large values of HR compared to their long companions (Tavani, 1998; Fishman & Meegan, 1995). Furthermore, HR is found to be correlated with T_{90} for the complete sample of GRBs. However, no correlation is noticed between the two for an individual class (Qin et al., 2000).

Another characteristic is the spectral lag (i.e., the delay in the arrival times of low-energy photons to high-energy photons) which can differentiate the two classes. Long GRBs have significant lags (up to a few seconds for some of them) in their light curves in different energy channels. On the other hand, no lag (nearly

zero) is observed for short GRBs (Cheng et al., 1995; Yi et al., 2006; Kaneko et al., 2015).

The two classes can also be compared concerning their energetics ($E_{\gamma, \text{iso}}$) and luminosities ($L_{\text{p}, \text{iso}}$). Short GRBs have, on average, energies that are smaller than that of long bursts (Ghirlanda et al., 2009). They are located at two different places in $E_{\gamma, \text{iso}} - E_{\text{p}}$ plane (Amati plane), following a correlation that is parallel to each other (Amati et al., 2002; Amati, 2006). Additionally, the host galaxy properties such as stellar population, star formation rate (SFR), morphology, offset, etc., are different for short and long bursts in general and can provide a clue about the burst progenitor system and hence the class of the GRB (Li et al., 2016).

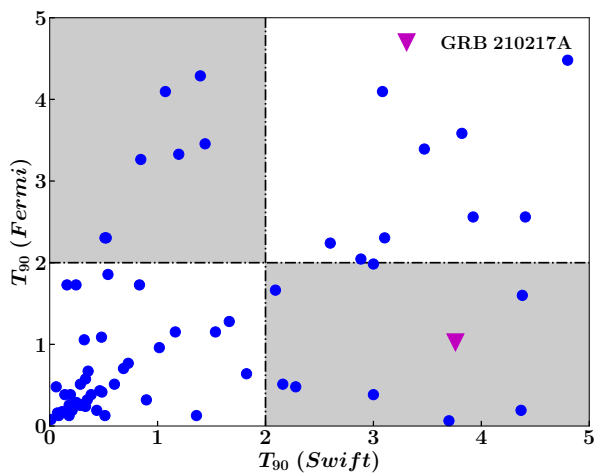


Figure 1. T_{90} duration of GRBs detected by both *Fermi* (50-300 keV) and *Swift* (15-350 keV). GRBs lying in the first and third quadrant have the same classification from both satellites. However, GRBs lying in the second and fourth quadrant (shaded grey region) have different classifications from both satellites. The magenta triangle represents GRB 210217A.

The sensitivity of detectors affects the duration timescales of the bursts. As a result, GRBs detected by *Swift* and *Fermi* have different values of duration reported. Figure 1 represents the T_{90} values as measured by *Swift* (15-350 keV) and *Fermi* (50-300 keV). The bursts have different values of T_{90} reported by *Swift* and *Fermi*. Most of them are lying in the same class, either short or long burst (first and third quadrant). There are 16 GRBs detected by *Swift* and *Fermi* between 2008 to February 2021, including GRB 210217A (second and fourth quadrant, the shaded grey regions), having different classification provided by two satellites.

GRB 210217A is one of the recent bursts lying at the boundary of short and long GRBs divide with different burst duration values reported by *Swift* and *Fermi*. GRB 210217A was detected by *Swift*-BAT (Simpson

et al., 2021) and *Fermi*-GBM (Fletcher & *Fermi*-GBM Team, 2021). *Swift* Burst alert telescope (BAT) reported a T_{90} of 4.22 ± 1.15 sec (15-350 keV), suggesting it to be a long GRB (Sakamoto et al., 2021). The sub-threshold detection by *Fermi*-GBM with a duration of 1.024 sec (25-294 keV) suggests that the burst might belong to the short population of GRBs¹. This burst was well within the observational capabilities of moderate-sized Indian telescopes. Therefore, we observed the optical afterglow of this burst with the 1.3m Devasthal Fast Optical Telescope (DFOT) and 3.6m Devasthal Optical Telescope (DOT) located in Aryabhata Research Institute of Observational Sciences (ARIES), Nainital. The study of prompt and afterglow emission of a GRB provides a complete picture of the nature of the GRB.

We performed a detailed analysis to classify GRB 210217A. This paper presents the multi-wavelength analysis of GRB 210217A and discusses various methods for classification. Further, we estimated the burst's redshift using joint fitting of the spectral energy distribution (SED) obtained from UVOT/XRT afterglow. In section 2, we describe the discovery and follow-up observations of GRB 210217A. The data acquisition and reduction procedures are explained in section 3. Section 4 presents the results obtained and a discussion on the possible classification of GRB 210217A. Finally, we summarise the conclusions of this work in Section 5. We used the Hubble parameter $H_0 = 70 \text{ km sec}^{-1} \text{ Mpc}^{-1}$, density parameters $\Omega_{\Lambda} = 0.73$, and $\Omega_m = 0.27$ (Jarosik et al., 2011).

2. GRB 210217A

BAT on-board NASA's *Swift* space mission (Barthelmy et al., 2005) triggered GRB 210217A on 17th February 2021 at 23:25:42 UT and provided the location of the source with coordinates RA, and DEC = 06h 30m 26s, +68d 42' 53" (J2000) respectively with an uncertainty of 3 arcmin (Simpson et al., 2021). The *Swift* X-Ray Telescope (XRT) observations 97.8 seconds after the BAT trigger located an uncatalogued X-ray source at RA, and Dec = 06h 30m 20.82s, +68d 43' 29.9" (J2000) with an uncertainty of 3.7 arcseconds. *Swift* Ultra-Violet and Optical telescope (UVOT) observations at 103 seconds after the BAT trigger detected a transient in white and U filters.

Several ground-based optical/NIR telescopes started observing the field of GRB 210217A and re-

¹https://gcn.gsfc.nasa.gov/notices_gbm_sub/635297147.fermi

Table 1. Characteristics of GRB 210217A. T_{90} : Duration from *Swift*-BAT observations; Transient Duration: Duration of the transient reported by *Fermi*-GBM ; HR: Ratio of the fluence in 25-50 keV to that in 15-25 keV; t_{mvts} : minimum variability time scale in 15-350 keV; E_p : Peak energy as reported by *Fermi*-GBM team (Fletcher & *Fermi*-GBM Team, 2021); z : photometric redshift obtained by fitting UVOT/X-ray SED; $E_{\gamma,\text{iso}}$: Isotropic γ -ray energy calculated using the photometric redshift.

Characteristics	GRB 210217A	Detector
T_{90} (15-350 keV)	3.76 ± 0.26 sec	<i>Swift</i> -BAT
T_{100} (25-294 keV)	1.024	<i>Fermi</i> -GBM
HR	1.40 ± 0.02	<i>Swift</i> -BAT
t_{mvts} (sec)	0.512	<i>Swift</i> -BAT
Spectral lag (ms)	186^{+68}_{-65}	<i>Swift</i> -BAT
E_p	230	<i>Fermi</i> -GBM
Redshift (z)	$0.55^{+0.90}_{-0.40}$	<i>Swift</i> -XRT +UVOT
$E_{\gamma,\text{iso}}$ (erg)	$(2.61 \pm 1.4) \times 10^{51}$	<i>Swift</i> -BAT

Table 2. T_{90} value of GRB 210217A in different energy channels

Energy range (keV)	T_{90} (sec)
15 – 350	3.76 ± 0.26
15 – 25	4.17 ± 0.12
25 – 50	3.78 ± 0.14
50 – 100	3.49 ± 0.72
100 – 350	3.79 ± 0.26

ported the optical afterglow magnitudes². *Fermi*-GBM did not trigger the event automatically (Fletcher & *Fermi*-GBM Team, 2021). Still, an automated, blind search for short GRBs (below the onboard triggering threshold) in *Fermi*-GBM identified a short GRB consistent with the *Swift*-BAT event in both time and location with a high significance value with a duration of 1.024 sec (Fletcher & *Fermi*-GBM Team, 2021).

We also carried out the observations of the optical afterglow of GRB 210217A with 1.3m DFOT located in ARIES at the earliest available opportunity (Kumar et al., 2021). Once the afterglow crosses the limit of

1.3m DFOT, we carried out deep observations with the 3.6m DOT (Dimple et al., 2021). The characteristics of the burst are presented in Table 1.

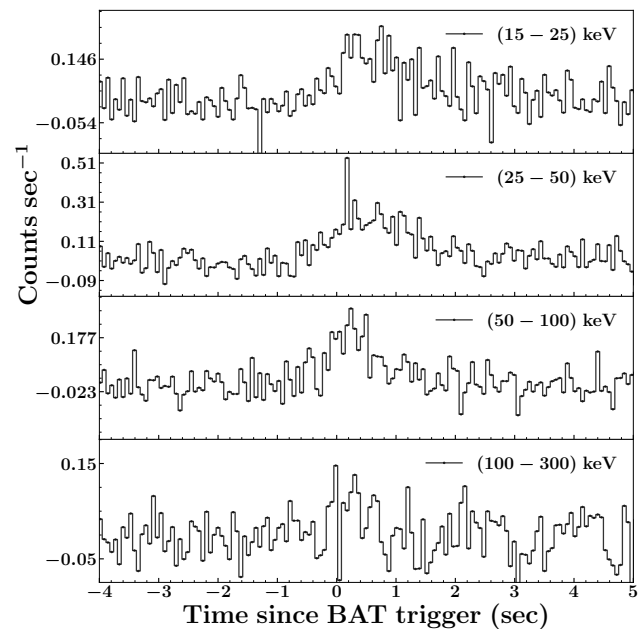


Figure 2. Background subtracted *Swift*-BAT count rate light curve of GRB 210217A in different energy channels with a time resolution of 64 ms.

²<https://gcn.gsfc.nasa.gov/other/210217A.gcn3>

Table 3. AB magnitudes of the afterglow of GRB 210217A along with the magnitudes reported in the GCN circulars. Magnitudes are not corrected for Galactic extinction. All the upper limits are given with 3 sigma value.

Δt (days)	Filter	Magnitude	Telescope	Reference
0.0021	White	18.80 ± 0.06	<i>Swift</i> -UVOT	This Work
2.2396	White	22.42 ± 0.35	<i>Swift</i> -UVOT	This Work
0.0048	U	18.75 ± 0.16	<i>Swift</i> -UVOT	This Work
0.75375	R	21.80 ± 0.08	1.3m DFOT	This Work
0.8220	I	21.56 ± 0.12	1.3m DFOT	This Work
1.7010	r	22.32 ± 0.16	3.6m DOT	This Work
2.7401	r	> 22.60	3.6m DOT	This Work
0.17791	R	20.80 ± 0.30	KAIT	Zheng et al. (2021)
0.0100	z	18.67 ± 0.10	2.0m Liverpool	Shrestha et al. (2021)
0.00120	r	18.60 ± 0.20	2.0m Liverpool	Shrestha et al. (2021)
0.0080	i	18.77 ± 0.10	2.0m Liverpool	Shrestha et al. (2021)

3. Data Acquisition and Reduction

This section narrates the data acquisition and analysis from different space missions and ground-based telescopes as part of the present work. The *Fermi*-GBM data is not publicly available for GRB 210217A as this burst was detected below the onboard triggering threshold³. For the rest of the work we used the parameters provided by the *Fermi*-GBM team^{4,5}.

3.1 *Swift*-BAT

To extract the temporal and spectral properties of GRB 210217A in high energy bands, the raw data of *Swift*-BAT (Observation Id: 01033264000) is obtained from the online portal of *Swift* Archive⁶. We reduced the data utilising the HEASOFT (version-6.25). The inbuilt pipelines *batbinevt*, *bathotpix*, and *batmaskwtevt* are used to create detector plane image (DPI) followed by removal of hot pixels and mask weighting. Later, the mask-weighted BAT light curves are extracted using *batbinevt* pipeline for different energy channels. The light curves in different energy channels are shown in Figure 2. Further, we estimated the T_{90} duration of light curves in different energy chan-

nels and are tabulated in Table 2. The T_{90} value in the energy range 15-350 keV is 3.76 ± 0.26 which is consistent with the value reported in Sakamoto et al. (2021).

To examine the spectral properties of the burst, we extracted the time-averaged BAT spectrum for the total duration of the burst starting from $T_0 - 0.065$ to $T_0 + 0.489$ sec (the start and end time of the pulse are identified using Bayesian binning of the light curve in the energy range 15-350 keV).

We used the *batbinevt* and *batdrngen* pipelines to produce the spectrum and detector response matrix (DRM), respectively. The resultant spectrum is fitted with the power-law and the cutoff power-law using the Multi-Mission Maximum Likelihood framework (3ML) package (Vianello et al., 2015). Maximum likelihood estimation technique was used for choosing the best fit model. We got the maximum value for likelihood for a single power-law model with photon index (Γ_{BAT}) of 1.99 ± 0.09 . The fluence is $6.7 \pm 0.39 \times 10^{-7} \text{ erg cm}^{-2}$ in the 15-150 keV band, which is consistent with the value reported by (Sakamoto et al., 2021).

3.2 *Swift*-XRT & UVOT

We obtained the X-ray flux light curve data in the 0.3-10 keV energy band from *Swift*-XRT Burst Analyser repository⁷ hosted by the University of Leicester (Evans et al., 2009). The flux light curve is then converted to flux density at 5 keV using the relations given

³https://gcn.gsfc.nasa.gov/fermi_gbm_subthresh_archive.html

⁴https://gcn.gsfc.nasa.gov/fermi_gbm_subthreshold.html

⁵https://gcn.gsfc.nasa.gov/notices_gbm_sub/635297147.fermi

⁶https://www.swift.ac.uk/swift_portal/

⁷<https://www.swift.ac.uk/>

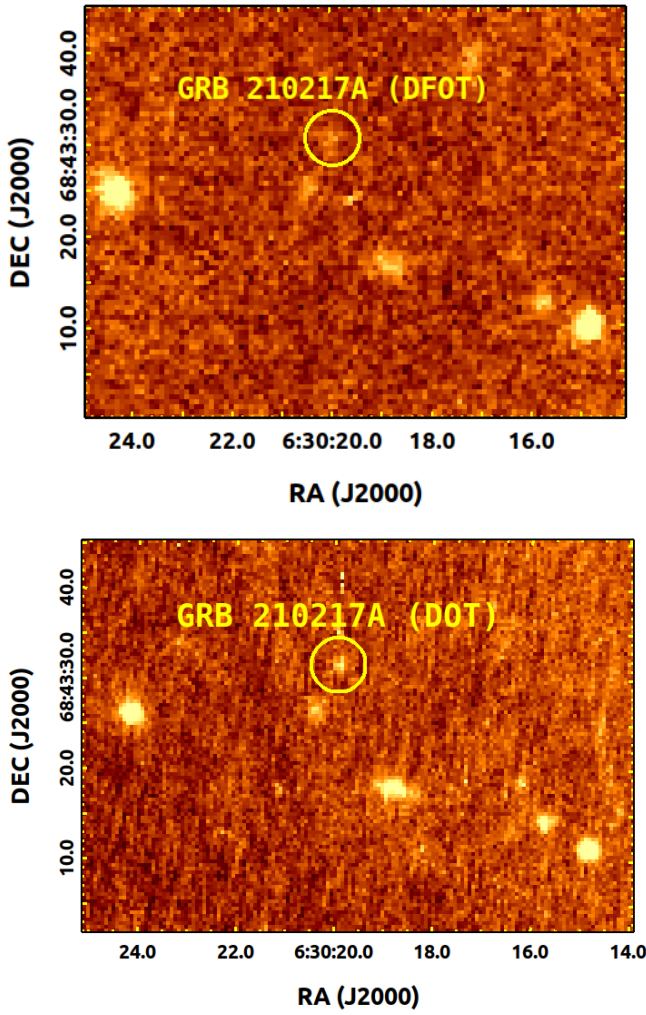


Figure 3. The optical finding chart of GRB 210217A taken with 1.3m DFOT (left) and 3.6m DOT (right) telescopes. The afterglow is visible, and its position is marked with yellow circles.

by Gehrels et al. (2008) for further analysis.

$$F_{\nu, x} = 4.13 \times 10^{11} \frac{F_x(2 - \Gamma_x)E_0^{1-\Gamma_x}}{E_2^{2-\Gamma_x} - E_1^{2-\Gamma_x}}. \quad (1)$$

where, E_1 and E_2 are lower and upper bounds of band pass in keV, E_0 is the energy in keV at which flux density is calculated, Γ_x is the X-ray photon index. F_x is the measured flux in $\text{erg cm}^{-2} \text{sec}^{-1}$.

We downloaded the *Swift*-UVOT data from the online *Swift* data archive page⁸. We analyzed the UVOT data using standard pipeline `uvotproduct` of `heasoft` software version 6.25 with the latest calibra-

tion database. A source region of 5 arcsec and a background region of 25 arcsec aperture radius are extracted for the photometric analysis of the burst. We detected a source in white and U filter. Table 3 shows the magnitudes of the source in these filters.

3.3 1.3m DFOT and 3.6m DOT

We started observations with 1.3 DFOT on 2021-02-18 at 17:31:22 UT located at Devasthal observatory of ARIES, India, for the follow-up observations of the optical afterglow of GRB 210217A. We observed a set of 30 images with an exposure of 120s each in the Bessel R filter and a set of 20 images (120s exposure) in the Bessel I filter. We detected the optical afterglow of GRB 210217A in the stacked frames within the *Swift* XRT error circle (left panel of Figure 3). Later, for deep observations, we observed the field with Aries Devasthal Faint Object Spectrograph and Camera (AD-FOSC) mounted on the 3.6m DOT around ~ 1.7 days after the burst. We took four consecutive images in r-band with an exposure of 900 sec each. We corrected the science images acquired from these telescopes for bias, flat and cosmic rays using *Astropy* module of Python.

We stacked the images to enhance the signal-to-noise ratio. The source is visible in stacked image (Dimple et al., 2021). The finding chart for the same is shown in the right panel of Figure 3. We used the DAOPHOT package to perform point spread function (PSF) photometry which was calibrated against the Panstarrs catalog resulting in apparent magnitudes listed in Table 3. The magnitudes are converted to flux density after correcting for galactic extinction. Figure 4 shows the multi-band light curve of GRB 210217A constructed using our data and those reported in GCN circulars.

Further, we fitted the X-ray and optical R band light curves of GRB 210217A using a single power law of the form $F = F_0 t^{-\alpha}$, where t corresponds to time, and α is the decay index. Due to the limited number of data points in other optical bands, it is not possible to fit these. Therefore, We overplotted the light curves in other bands using the R band decay index. The light curves with power laws are shown in Figure 4.

4. Results and Discussions

This section presents the results obtained from the multi-band analysis and possible classification scenario of GRB 210217A.

⁸<http://swift.gsfc.nasa.gov/docs/swift/archive/>

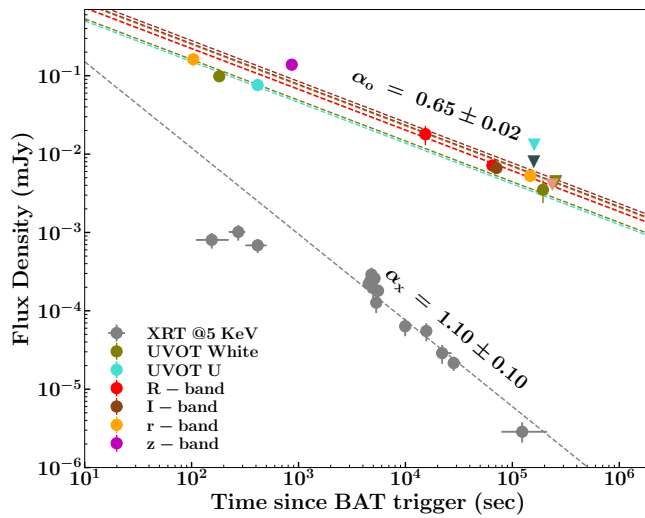


Figure 4. Multiwavelength afterglow light curves of GRB 210217A. Optical data points are corrected for galactic extinction. The X-ray data (shown in grey) are taken from *Swift*-XRT page. The best fit models are also shown with dashed lines.

4.1 Photometric Redshift

To estimate the photometric redshift of GRB 210217A, we analyzed the joint XRT and UVOT SED in the time interval of ~ 100 -200 sec. We didn't observe any spectral evolution during this time interval. Using the XRT data and UVOT magnitudes, we created the SED following the methodology described in [Chand et al. \(2020\)](#); [Gupta et al. \(2021\)](#). We fitted the SED using power-law and broken power-law models using XSPEC ([Arnaud, 1996](#)). The Galactic and intrinsic absorber components (phabs and zphabs) are also included from XSPEC models. The Galactic absorption is fixed to $N_{\text{H,Gal}} = 8.69 \times 10^{20} \text{cm}^{-2}$ ([Willingale et al., 2013](#)). We further included two dust components using the XSPEC model zdust, one at redshift $z=0$ for galactic dust component, and the other for the intrinsic dust component with varying redshift which provided the redshift information. The Galactic reddening is fixed at 0.0847 (E(B-V)) conforming to the map of [Schlafly & Finkbeiner \(2011\)](#). The SED is fitted with Milky Way, Large and Small Magellanic Clouds (MW, LMC, and SMC) extinction laws ([Pei, 1992](#)) at the redshift of the burst. Although all these models well explain the SED, a minimum χ^2 value is obtained for Milky way extinction law with a power-law model. The value of the spectral index is 1.85 ± 0.13 , and that of photometric redshift is $0.55^{+0.9}_{-0.4}$ for GRB 210217A. The SED is shown in Figure 5.

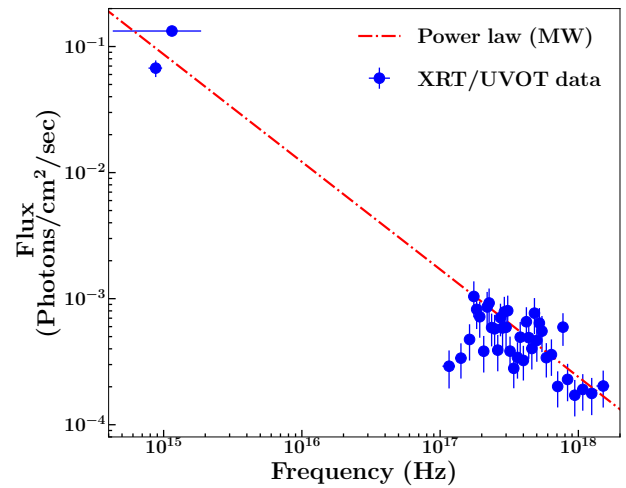


Figure 5. The SED obtained using joint *Swift* UVOT and XRT afterglow data for GRB 210217A. Data points are shown using blue circles. The SED is best fitted with a power-law model (shown with red dashed dotted line) with Milky way extinction law.

4.2 Hardness Ratio and Peak Energy

We estimated the HR using fluence ratio in two different energy channels: 15-25 keV and 50-100 keV energy bands of *Swift*-BAT and used it for the classification of GRB 210217A. The HR during T_{90} is found to be 0.64 ± 0.005 . We collected the sample of GRBs from *Swift*-BAT catalog⁹ and estimated the hardness ratio using the fluence in the same energy window as used for GRB 210217A. We fitted this sample with the Bayesian Gaussian mixture model (BGMM), which is a machine learning algorithm supported by scikit-learn ([Pedregosa et al., 2011](#)). Using this algorithm, we estimated the probability of GRB 210217A being a short GRB as 98.2%. The probabilities of the whole sample being a short GRB along with GRB 210217A are shown in Figure 6 (a).

As *Swift* BAT has narrow spectral coverage, we could not determine E_p using spectral fitting. Therefore, we used the E_p , peak energy and T_{90} values provided by *Fermi*-GBM along with the E_p - T_{90} values from the *Fermi*-GBM catalog to identify the class of GRB 210217A. We again fitted the distribution with BGMM and found a probability of 96% for GRB 210217A being a short GRB. The probability map is shown in Figure 6 (b).

⁹https://swift.gsfc.nasa.gov/results/batgrbcat/summary_cflux/summary_T100/summary_pow_energy_fluence.txt

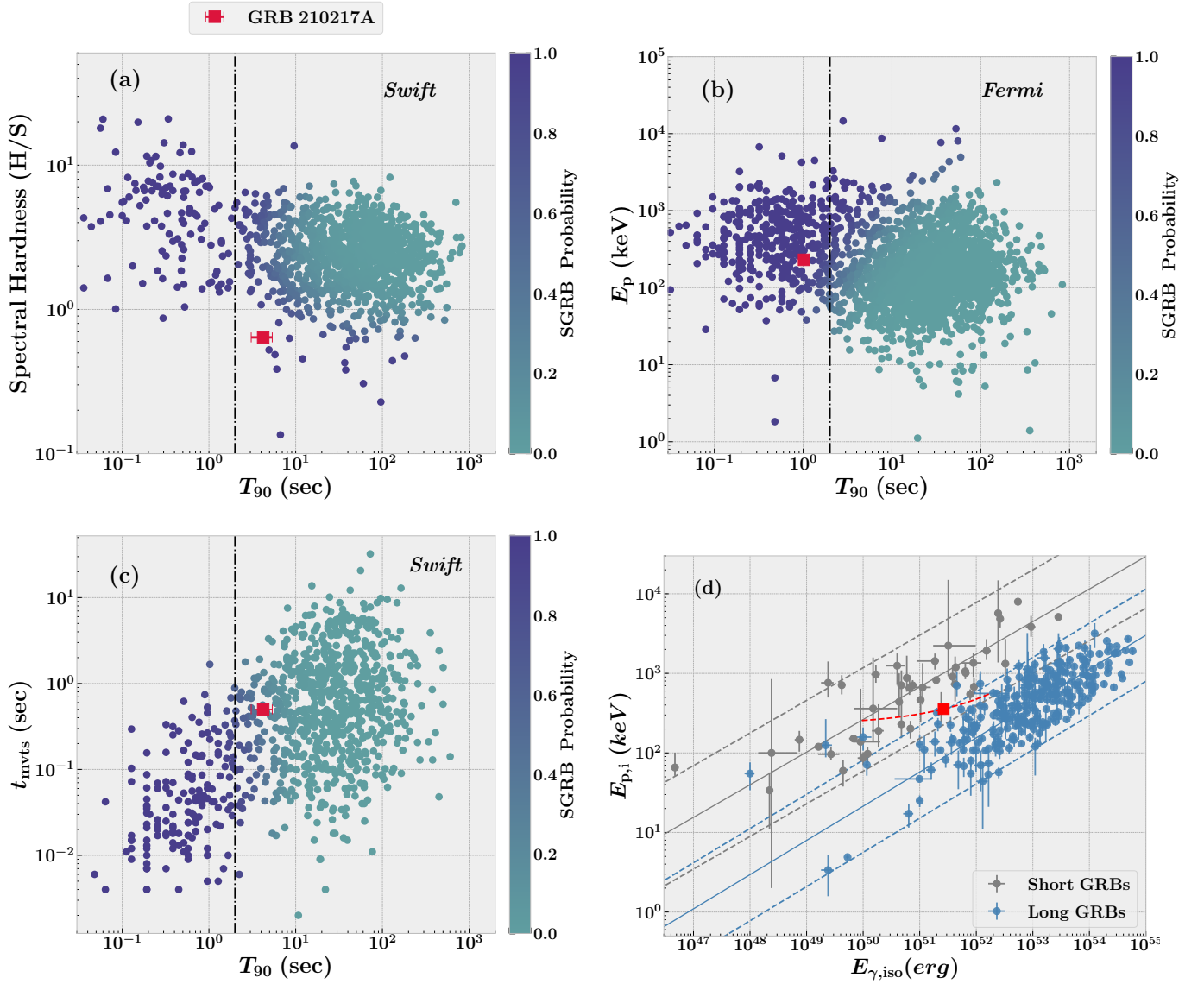


Figure 6. (a) The spectral hardness and T_{90} for GRB 210217A (shown with a red square) along with the GRB sample (for short and long GRBs) presented in Goldstein et al. (2017). (b) GRB 210217A in E_p - T_{90} plane with the dataset available from *Fermi*-GBM catalog. (c) Minimum variability time scale (t_{mvts}) as a function of T_{90} for GRB 210217A along with the short and long GRBs sample studied by Golkhou et al. (2015). The colour scale on the right side of the Figure shows the probability of the GRB being a short GRB and the vertical dashed line at 2 sec shows the boundary separating the short and long classes of GRB. (d) GRB 210217A in the Amati plane along with the data points for long and short GRBs taken from Minaev & Pozanenko (2020). The solid lines shows the best correlation between $E_{p,i} - E_{\gamma,\text{iso}}$ along with 2-sigma correlation presented by dashed line of respective colors for short (grey) and long class (steelblue). $E_{p,i} - E_{\gamma,\text{iso}}$ for GRB 210217A is shown with a red square. The red dashed line show the $E_{p,i} - E_{\gamma,\text{iso}}$ for the redshift range considering the uncertainty in photometric redshift.

4.3 Minimum variability time scale

High energy light curves of GRBs are highly variable and can be explained with the GRB central engine resulting from internal shocks. Hence, minimum variability time scale (MacLachlan et al., 2013, t_{mvts}) gives an idea about the central engine, the source emission radius (R_c), and the minimum Lorentz factor (Sonbas

et al., 2015, Γ_{min}) of GRBs. In general, the t_{mvts} value for long bursts is larger with an average value of 200 ms than their short counterparts having a mean value of 10 ms, indicating that short GRBs have a more compact central engine (MacLachlan et al., 2012, 2013). We measured the t_{mvts} for GRB 210217A using the method described in Golkhou et al. (2015). The estimated value of t_{mvts} is ~ 0.512 sec for GRB 210217A, which we fur-

ther used for its classification. We collected t_{mvts} values for short and long GRB samples from [Golkhou et al. \(2015\)](#). Using BGMM, we found the probability of GRB 210217A being a short GRB equal to 28% (Figure 6 (c)).

4.4 Spectral lag

We calculated the spectral lag using bat light curves in energy channels; 15-25 keV and 50-100 keV. We estimated the using the cross-correlation function (CCF) and uncertainties in the CCF following the method described in [Bernardini et al. \(2015\)](#). We fitted the CCF with an asymmetric Gaussian function using *emcee* ([Foreman-Mackey et al., 2013](#)) to find its global maximum, which represents the lag in two light curves. We found a positive lag 86^{+68}_{-65} ms for the burst. The average value of lag for short and long GRBs are 16.5 ± 7.5 and 375.1 ± 69.6 ms, respectively ([Bernardini et al., 2015](#)). The value is lying more close to the mean value of short GRBs within the errorbar. With the intermediate value of spectral lag lying between the mean value of two classes, it is hard to classify the burst.

4.5 Amati correlation

We also used the well-known correlation between the isotropic equivalent energy emitted in the high energy regime, $E_{\gamma,\text{iso}}$ and E_p (the energy at which νF_ν is maximum) to classify GRB 210217A ([Amati et al., 2002](#); [Amati, 2006](#); [Minaev & Pozanenko, 2020](#)). A power-law well fits this correlation with an index of $a \simeq 0.4$; however, the correlation regions are well separated for different classes ([Minaev & Pozanenko, 2020](#)).

For the redshift range (0.15-1.45) obtained from SED (section 4.1), we estimated the $E_{\gamma,\text{iso}}$ using the following equation 2

$$E_{\gamma,\text{iso}} = K_{\text{bol}} \times \frac{4\pi d_L^2}{1+z} f_\gamma. \quad (2)$$

where, K_{bol} is the bolometric correction factor, d_L is the luminosity distance and f_γ is the fluence (erg cm^{-2}). For *Swift*-BAT energy range (15-150 keV) we used $K_{\text{bol}} = 5$ ([Fong et al., 2015](#)) and the fluence value calculated in section 3.1. We also estimated the $E_{p,i}$ (peak energy in the source frame) for the estimated redshift range. As *Swift*-BAT covers only a small energy range, we used the E_p and burst duration as reported by *Fermi*-GBM team ([Fletcher & Fermi-GBM Team, 2021](#)). The red dashed line in the Figure 6 (d) shows the $E_{\gamma,\text{iso}} - E_{p,i}$ for the redshift range of GRB 210217A. GRB 210217A lies in the region in between long and short GRBs.

5. Summary

We report a detailed analysis of GRB 210217A using publicly available multi-wavelength observations, including our observations from our ARIES telescopes. We try to find the true class of GRB 210217A using various methods described in the literature. We calculated the photometric redshift using *Swift*-XRT/UVOT data. Using this estimated redshift, we calculated the isotropic equivalent energy and peak energy in the source frame. GRB 210217A lies at the boundary between short and long class in the Amati plane.

We also calculated the HR, minimum variability timescale, spectral lag and fitted the T_{90} -HR, T_{90} -Ep, T_{90} -mvts distribution using BGMM. We found a probability of GRB 210217A being a short GRB equal to 98.2%, 96%, and 28% in these cases, respectively. It is hard to conclude if GRB 210217A belongs to the long or the short class as some of the properties belong to long GRBs and others to short.

The host studies can clarify the true class of this burst. The fact that two categories have different progenitors, they are originated in different kinds of host galaxies. Long GRBs are located in the star-forming young population of galaxies; the short GRBs belongs to the old population of galaxies ([Li et al., 2016](#)). Long GRBs are generally located in bright star-forming regions with minimal offsets from the centre of the host galaxy on a galactic scale. In contrast, due to significant merger scale times, short GRBs have large offsets from the centre of their galaxies ([Bloom et al., 2002](#); [Fong et al., 2013](#)). The host observations are not available for GRB 210217A. However, the host observations can give a clue about the class of GRB 210217A.

Acknowledgements

KM, RG, and SBP acknowledge BRICS grant DST/IMRCD/BRICS/PilotCall1/ProFCheap/2017(G) for the financial support. KGA is partially supported by the Swarnajayanti Fellowship Grant No.DST/SJF/PSA-01/2017-18, MATRICS grant MTR/2020/000177 of SERB, and a grant from the Infosys Foundation. This research is based on observations obtained at the 3.6m Devasthal Optical Telescope (DOT) during observing cycles DOT-2021-C1, a National Facility runs and managed by Aryabhata Research Institute Observational Sciences (ARIES), an autonomous Institute under the Department of Science and Technology, Government of India. This research has used data obtained from the High Energy Astrophysics Science Archive Research Center (HEASARC) and the Leicester Database and Archive Service (LEDAS),

provided by NASA's Goddard Space Flight Flight Center and the Department of Physics and Astronomy, Leicester University, UK, respectively.

References

- Ahumada, T., Singer, L. P., Anand, S., et al. 2021, *Nature Astronomy*. doi:10.1038/s41550-021-01428-7
- Amati, L., Frontera, F., Tavani, M., et al. 2002, *Astronomy and Astrophysics*, 390, 81. doi:10.1051/0004-6361:20020722
- Amati, L. 2006, *MNRAS*, 372, 233. doi:10.1111/j.1365-2966.2006.10840.x
- Antonelli, L. A., D'Avanzo, P., Perna, R., et al. 2009, *Astronomy and Astrophysics*, 507, L45. doi:10.1051/0004-6361/200913062
- Arnaud, K. A. 1996, *Astronomical Data Analysis Software and Systems V*, 101, 17
- Barthelmy, S. D., Barbier, L. M., Cummings, J. R., et al. 2005, *Space Science Reviews*, 120, 143. doi:10.1007/s11214-005-5096-3
- Bernardini, M. G., Ghirlanda, G., Campana, S., et al. 2015, *MNRAS*, 446, 1129. doi:10.1093/mnras/stu2153
- Bloom, J. S., Kulkarni, S. R., & Djorgovski, S. G. 2002, *AJ*, 123, 1111. doi:10.1086/338893
- Breeveld, A. A., Landsman, W., Holland, S. T., et al. 2011, *Gamma Ray Bursts 2010*, 1358, 373. doi:10.1063/1.3621807
- Chand, V., Banerjee, A., Gupta, R., et al. 2020, *ApJ*, 898, 42. doi:10.3847/1538-4357/ab9606
- Cheng, L. X., Ma, Y. Q., Cheng, K. S., et al. 1995, *Astronomy and Astrophysics*, 300, 746
- Dimple, Misra, K., Ghosh, A., et al. 2021, GRB Coordinates Network, Circular Service, No. 29591, 29591
- Evans, P. A., Beardmore, A. P., Page, K. L., et al. 2009, *MNRAS*, 397, 1177. doi:10.1111/j.1365-2966.2009.14913.x
- Fenimore, E. E., in 't Zand, J. J. M., Norris, J. P., et al. 1995, *ApJL*, 448, L101. doi:10.1086/309603
- Fishman, G. J. & Meegan, C. A. 1995, *ARAA*, 33, 415. doi:10.1146/annurev.aa.33.090195.002215
- Fletcher, C. & Fermi-GBM Team 2021, GRB Coordinates Network, Circular Service, No. 29536, 29536
- Fong, W., Berger, E. and Chornock, R. et al. 2013, *ApJ*, 769, 1.
- Fong, W. and Berger, E. and Margutti, R. et al. 2015, *ApJ*, 102. doi:10.1088/0004-637x/815/2/102
- Foreman-Mackey, D., Hogg, D. W., Lang, D., et al. 2013, *pasp*, 125, 306. doi:10.1086/670067
- Gal-Yam, A., Fox, D. B., Price, P. A., et al. 2006, *Nature*, 444, 1053. doi:10.1038/nature05373
- Gehrels, N., Barthelmy, S. D. and Burrows, D. N. et al. 2008, *ApJ*, 689, 2. doi: 10.1086/592766.
- Ghirlanda, G., Nava, L., Ghisellini, G., et al. 2009, *Astronomy and Astrophysics*, 496, 585. doi:10.1051/0004-6361/200811209
- Goldstein, A., Veres, P., Burns, E., et al. 2017, *ApJL*, 848, L14. doi:10.3847/2041-8213/aa8f41
- Golkhou, V. Z., Butler, N. R., & Littlejohns, O. M. 2015, *ApJ*, 811, 93. doi:10.1088/0004-637X/811/2/93
- Gupta, R., Oates, S. R., Pandey, S. B., et al. 2021, *MNRAS*, 505, 4086. doi:10.1093/mnras/stab1573
- Jarosik, N., Bennett, C. L., Dunkley, J., et al. 2011, *ApJS*, 192, 14. doi:10.1088/0067-0049/192/2/14
- Kaneko, Y., Bostancı, Z. F., Göğüş, E., et al. 2015, *MNRAS*, 452, 824. doi:10.1093/mnras/stv1286
- Kouveliotou, C., Meegan, C. A., Fishman, G. J., et al. 1993, *ApJL*, 413, L101. doi:10.1086/186969
- Qin, Y.-P. & Chen, Z.-F. 2013, *MNRAS*, 430, 163. doi:10.1093/mnras/sts547
- Kumar, A., Gupta, R., Ghosh, A., et al. 2021, GRB Coordinates Network, Circular Service, No. 29539, 29539
- Li, Y., Zhang, B., & Lü, H.-J. 2016, *ApJS*, 227, 7. doi:10.3847/0067-0049/227/1/7
- MacLachlan, G. A., Shenoy, A., Sonbas, E. et al. 2012, *MNRAS*, 425, L32-L35. doi: 10.1111/j.1745-3933.2012.01295.x
- MacLachlan, G. A., Shenoy, A., Sonbas, E., et al. 2013, *MNRAS*, 432, 857. doi:10.1093/mnras/stt241
- Minaev, P. Y. & Pozanenko, A. S. 2020, *MNRAS*, 492, 1919. doi:10.1093/mnras/stz3611

- Minaev, P. Y. & Pozanenko, A. S. 2020, *Astronomy Letters*, 46, 573. doi:10.1134/S1063773720090042
- Norris, J. P. 2002, *ApJ*, 579, 386. doi:10.1086/342747
- Pedregosa, F. and Varoquaux, G. et al. 2011, *JMLR*, 12, 2825–2830.
- Pei, Y. C. 1992, *ApJ*, 395, 130. doi:10.1086/171637
- Piran, T. 1999, *Physics Reports*, 314, 575. doi:10.1016/S0370-1573(98)00127-6
- Piran, T. 2004, *Reviews of Modern Physics*, 76, 1143. doi:10.1103/RevModPhys.76.1143
- Qin, Y.-P., Xie, G.-Z., Xue, S.-J., et al. 2000, *PASJ*, 52, 759. doi:10.1093/pasj/52.5.759
- Sakamoto, T., Barthelmy, S. D., Cummings, J. R., et al. 2021, GRB Coordinates Network, Circular Service, No. 29534, 29534
- Sari, R., Piran, T., & Narayan, R. 1998, *ApJL*, 497, L17. doi:10.1086/311269
- Schlaflly, E. F. & Finkbeiner, D. P. 2011, *ApJ*, 737, 103. doi:10.1088/0004-637X/737/2/103
- Shrestha, M., Smith, R., Melandri, A., et al. 2021, GRB Coordinates Network, Circular Service, No. 29535, 29535
- Simpson, K. K., Gropp, J. D., Kennea, J. A., et al. 2021, GRB Coordinates Network, Circular Service, No. 29521, 29521
- Sonbas, E., MacLachlan, G. A., Dhuga, K. S., et al. 2015, *ApJ*, 805, 86. doi:10.1088/0004-637X/805/2/86
- Tavani, M. 1998, *ApJL*, 497, L21. doi:10.1086/311276
- Vianello, G., Lauer, R. J., Younk, P., et al. 2015, arXiv:1507.08343
- Willingale, R., Starling, R. L. C. and Beardmore, A. P., et al. 2013, *MNRAS*, 431, 394-404. doi:10.1093/mnras/stt175
- Yi, T., Liang, E., Qin, Y., et al. 2006, *MNRAS*, 367, 1751. doi:10.1111/j.1365-2966.2006.10083.x
- Zheng, W., Filippenko, A. V., & KAIT GRB Team 2021, GRB Coordinates Network, Circular Service, No. 29533, 29533

6. Appendix

6.1 Afterglow Properties

The afterglow of the GRB can be well explained by the synchrotron fireball model (Piran, 1999). The spectra, as well as the light curves, consist of a combination of power-law and broken power-law characterized by electron distribution index p (Piran, 2004; Sari et al., 1998). We used the spectral and temporal indices to constrain p and the break frequencies using well-known closure relations (Sari et al., 1998). For this purpose, we fitted the X-ray and optical light curves/spectra at different epochs with single and broken power-law models. Both X-ray and optical light curves are well explained with a single power with indices value of 1.10 ± 0.1 and 0.65 ± 0.02 , respectively. The values of spectral indices at different epochs are given in Table 4. At around 0.3 ks, the spectral index is almost the same for optical and X-ray within the errorbar, suggesting no cooling break between X-ray to optical data. However, we found that the X-ray spectral index is almost two times the optical index at later epochs, indicating some break. So, we further created the spectral energy distributions using optical and X-ray data at two epochs centred at ~ 0.27 ks and ~ 125 ks. We fitted the SEDs with power-law and broken power-law models. The SED at the early epoch is best fitted with a single power-law with an index of 0.607 ± 0.02 . However, the SED at the later epoch is best fitted with a broken power-law with indices $0.65^{+0.08}_{-0.07}$ (pre-break) and $1.32^{+0.28}_{-0.21}$ (post-break) and a break at $1.7 \pm 0.3 \times 10^{17}$ Hz, which we identify as a cooling break. The best-fitted SEDs are shown in Figure 7.

Table 4. Optical and X-ray spectral indices obtained from fitting SEDs at different epochs and their best describe spectral regime. p is the mean value of the electron distribution indices calculated using temporal and spectral indices in that spectral regime

Time interval (s)	β_{opt}	$\beta_{\text{x-ray}}$	p (Spectral regime)
$0.5\text{--}5 \times 10^2$	$0.61^{+0.03}_{-0.02}$	$0.89^{+0.32}_{-0.30}$	2.00 ± 0.35 ($\nu_{\text{opt}} < \nu_{\text{x-ray}} < \nu_{\text{c}}$)
$6.5\text{--}19.3 \times 10^4$	$0.65^{+0.08}_{-0.07}$	$1.32^{+0.28}_{-0.21}$	2.43 ± 0.36 ($\nu_{\text{opt}} < \nu_{\text{c}} < \nu_{\text{x-ray}}$)

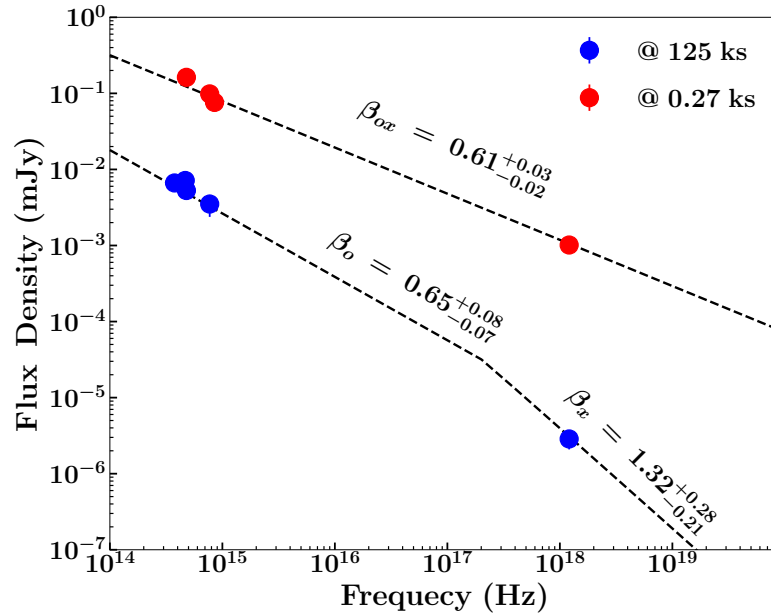


Figure 7. The optical/X-ray SEDs at two different epochs (~ 270 sec and at ~ 1.45 days after the trigger). The SED at the earlier epoch is well fitted with a simple power-law with a spectral index of $0.61^{+0.03}_{-0.02}$. However, a spectral break can be seen at the later epoch which is identified as the synchrotron cooling break.